Composite Structures 381 (2026) 120023

Contents lists available at ScienceDirect

Composite Structures

journal homepage: www.elsevier.com/locate/compstruct

Steering for in-situ AFP-manufactured structures: Part 1 - Critical arc length

Lukas Raps *, Ashley R. Chadwick, Heinz F. Voggenreiter

German Aerospace Center (DLR) - Institute of Structures and Design, Pfaffenwaldring 38-40, 70569, Stuttgart, Germany

ARTICLE INFO

Keywords:
Automated Fiber Placement
In-situ consolidation
Thermoplastic composites
Steering

ABSTRACT

Automated Fiber Placement (AFP) of thermoplastic composites offers a pathway to efficient, Out-of-Autoclave (OoA) manufacturing of large aerospace structures. This work investigates the in-plane path curvature (steering) required for double-curved geometries and the following transient steering effects and defect formation. A novel "critical arc length" concept is introduced to define the limits of viable steered layup paths. Results demonstrate that sub-critical steering radii do not significantly impact interlaminar shear or bending strength, though a minor reduction in bending modulus is observed near the critical arc length, likely attributable to increased fiber waviness. These findings expand the design space for steered thermoplastic composite structures.

1. Introduction

The aerospace industry increasingly relies on carbon-fiber-reinforced polymer composites for primary aircraft structures. However, manufacturing bottlenecks related to costly autoclaves and mechanical fastening limit production scalability. Thermoplastic composites offer a potential solution through Out-of-Autoclave (OoA) processing and welding technologies. Recent material and automation advances have re-ignited interest in their use for large-scale structures. In-situ consolidation Automated Fiber Placement (AFP) represents a particularly promising, yet challenging, approach – aiming for direct, additive laminate manufacturing. While temperature controlled diode laser heating and AFP-grade prepreg materials have enabled near press consolidation quality properties in flat panels [1], extending this process to complex, double-curved geometries presents significant hurdles. Specifically, the interaction of layup strategy and part geometry leads to the formation of two primary defect types: coverage defects (gaps and overlaps) and in-plane path curvature (steering) defects. This research focuses on understanding and characterizing steering effects inherent in the in-situ AFP process for complex aircraft structures.

1.1. Thermoset steering

The majority of research results in the literature focus on thermoset AFP steering. However, the geometric effects can be transferred to thermoplastic AFP and a brief overview is presented below. Steering is the forced in-plane curvature of prepreg tape resulting from the layup path, which is dictated by the overall layup strategy. The local path curvature is determined by the surface geometry and the layup path C on the surface S. At any point P on the path, the curvature vector $\boldsymbol{K}$ can be calculated as:

$$\boldsymbol{K} = \frac{d\boldsymbol{t}}{ds} \tag{1}$$

where $\boldsymbol{t}$ is the tangent vector of the reference curve C at point P [2]. The curvature vector can be separated into geodesic ($\boldsymbol{K_g}$) and normal ($\boldsymbol{K_n}$) components, acting in the direction of the unit tangent vector $\boldsymbol{u}$ and the unit normal vector $\boldsymbol{n}$, respectively:

$$\boldsymbol{K} = \boldsymbol{K_g} + \boldsymbol{K_n} \tag{2}$$

The in-plane (geodesic) steering radius R is inversely proportional to the scalar value of the geodesic curvature:

$$R = \frac{1}{K_g} \tag{3}$$

Given that the tape thickness is significantly smaller than the tape width (thicknes/width <0.05 for typical 6.35 mm prepregs), the normal curvature component is negligible; geodesic curvature is therefore the primary driver of steering defects [2–4]. These defects arise from the induced difference in arc length between the inner and outer edges of the tape, resulting in tensile stress on the outer fibers and compressive stress on the inner fibers. As the tensile modulus of carbon fibers is approximately twice its compressive modulus [5], tensile strain does not occur to a significant extent. Instead, compressive stress at the inner tow edge results in compressive strain, buckling, and undulations. The compressive strain at the inner edge ϵ_c can therefore be calculated relative to an assumed unchanged length of the outer edge as [4,6]:

$$\epsilon_c = \frac{w_t}{R + w_t/2} \tag{4}$$

* Corresponding author.
E-mail address: lukas.raps@dlr.de (L. Raps).

https://doi.org/10.1016/j.compstruct.2025.120023
Received 15 June 2025; Received in revised form 22 December 2025; Accepted 30 December 2025
Available online 9 January 2026

Table 1
Thermoset AFP critical steering radii.

Tape width [mm]	Critical steering radius R_{crit} [mm]
3.175	500–635 [11–16]
6.35	1350–1778 [11,15]
12.7	8890 [15]

where w_t is the material tow width. Work by Belhaj and Hojjati [7] suggests that due to the high tensile modulus and buckling propensity of carbon fibers at the inner edge, a majority of the bending strain is compensated by compressive strain at the inner tape edge. Observations of a shifted neutral fiber of the steered tape towards the outer edge support this theory [7–9].

Literature reports critical minimum steering radii for defect-free thermoset AFP (Table 1). These radii serve as reference values, but are significantly influenced by material properties, process parameters (e.g., tape tension, nip point temperature), and equipment capabilities [10].

Steering-induced defects, as categorized by Bakhshi et al. [17], include in-plane fiber waviness, sheared fibers, tow pull-up, blisters and out-of-plane wrinkles. The formation of out-of-plane defects is generally initiated when the geometric curvature exceeds a critical threshold, beyond which in-plane deformation is insufficient to accommodate the strain.

Unlike thermoplastic AFP, where consolidation is achieved in the additive process, thermoset prepreg tackiness plays a crucial role in resisting out-of-plane buckling during steering [17–19]. Rajan et al. [20] observed a time-dependent increase in wrinkle amplitude in thermoset AFP parts due to the viscoelastic behavior of the prepreg tack, demonstrating almost a doubling of amplitude within one hour post-deposition while the wrinkle pattern remained consistent.

Numerous studies have focused on quantifying these defects. Methods range from qualitative visual inspection [11,17,21,22] and wavelength measurement [19] to more advanced techniques like digital image correlation (DIC) for characterizing wrinkle geometry [20] and laser line scanning [23].

Modeling efforts have addressed the prediction of out-of-plane wrinkling. Local approaches treat steered tape sections as orthotropic plates to analyze buckling behavior at unsupported edges [7,9,19,24,25], while global models consider the entire curved tape length [17,18,26,27]. For example, Wehbe et al. [26] developed a model assuming wrinkle formation concentrates at the inner tape edge to accommodate length discrepancies.

Beyond wrinkle formation, fiber straightening can occur after tow cuts, particularly at the outer radius of steered courses [12,28]. These studies suggest minimizing cuts at the outer radius and prioritizing cuts on the inner radius to mitigate this issue. Kim et al. [29–31] proposed an alternative approach using tow shearing with dry-fiber tape and resin film impregnation, achieving a significantly reduced steering radius (down to 30 mm) using a specially-developed shearing end effector. However, this technique is limited to total steering angles below 90° before requiring a reversed curved section.

1.2. Thermoplastic steering

Investigations into steering thermoplastic tapes using diode laser AFP have demonstrated both opportunities and challenges in achieving complex geometries. Zenker and Schwab [8] observed temperature gradients and in-plane fiber undulations during the steering of 6.35 mm carbon fiber/polyamide 6 (CF/PA6) tapes, attributing higher temperatures on the inner radius to increased deposition rate and reduced contact with the consolidation roller. This led to localized heat spots and compressive stress, manifesting as short wavelengths (down to 3 mm) at the inner edge. Subsequent work by Zenker and Gnaedinger [32] quantitatively linked lower steering radii to increased gap formation at the inner edge of CF/PA6 tapes using image analysis.

Clancy et al. [33] investigated steering effects on 6 mm and 6.35 mm CF/PEEK tapes, finding a correlation between decreasing steering radius and both reduced consolidated tape width and increased thickness. While a steering radius of 800 mm was achieved without visible defects, radii of 600 mm exhibited minor wrinkling, and radii of 400 mm or less resulted in increased out-of-plane defects and poor bond quality. Wedge peel testing indicated a reduction in consolidation strength with both increased layup speed and decreased steering radius, although the limited sample size ($n \leq 4$) warrants further investigation. Despite these challenges, the authors suggest that thermoplastic AFP offers comparable, or potentially improved, steering performance relative to thermoset and dry fiber placement techniques.

Rajasekaran and Shadmehri [34] investigated steering effects in thermoplastic AFP using a nitrogen hot gas torch for in-situ consolidation of 6.35 mm CF/PEEK tape. Their findings indicated successful steering without defects up to a radius of 600 mm, with buckling observed at 400 mm and severe folding defects at 200 mm. Consistent with prior work [33], steering resulted in reduced consolidated tape width and increased thickness. Lap shear testing demonstrated comparable bond strength for steered tapes (radii 400–1000 mm) to straight layups, though a significant reduction in strength was observed at the 200 mm radius. Layup speed was found to influence defect frequency, with higher speeds reducing buckling but compromising overall consolidation and lap shear strength. Substrate angle exhibited similar effects on both straight and steered laminates, with a slight linear decrease in performance observed with increasing angle from 0° to 90° .

An overview of steering results in thermoplastic AFP literature is presented in Table 2.

1.3. Novelty

Existing literature primarily focuses on identifying critical steering radii, which are the smallest steering radii without defects, an approach well-suited to thermoset AFP where defects develop from the force balance between tackiness of the uncured prepreg and compressive stress, often after the consolidation roller has passed. While this principle has been adopted for thermoplastic AFP, full consolidation is achieved in the thermoplastic AFP process and defects can only develop up to the point of consolidation. The defects arise as a function of the accumulated curvature up to the current point on the layup path. By leveraging the in-situ consolidation process and considering the transient onset of critical defects, this research introduces a novel critical arc length criterion expanding the usable design space for steered layup paths. The critical arc length was defined as the achievable defect-free arc length for steering radii smaller than the critical steering radius. The proposed principle was validated on laminate level for these radii smaller than the critical steering radius (sub-critical steering radii) through a multi-faceted approach employing non-destructive testing, microstructural analysis, and mechanical characterization of interlaminar shear strength and bending properties, up to the defined critical arc length.

2. Methodology

2.1. Manufacturing facility and parameters

Automated Fiber Placement (AFP) experiments were conducted utilizing the thermoplastic tape placement facility at the German Aerospace Center (DLR) Institute of Structures and Design (Fig. 1). The facility comprises a six-axis KR210 (KUKA AG, Augsburg, Germany) industrial robot integrated with a KUKA DKP-400 two-axis positioner and flat, heatable aluminum tooling. A multi tape laying head (MTLH) end-effector (AFPT GmbH, Doerth, Germany) was employed, capable

Table 2
Thermoplastic AFP steering experiments.

Ref	Material	AFP Process	Steering radii [mm]	Defect-free radius [mm]
[8]	CF/PA6 6.35	Diode laser	1200 - 200	–
[33]	CF/PEEK 6 - 6.35	Diode laser	2000 - 200	800
[34]	CF/PEEK 6.35	Nitrogen hot gas torch	1000 - 200	600

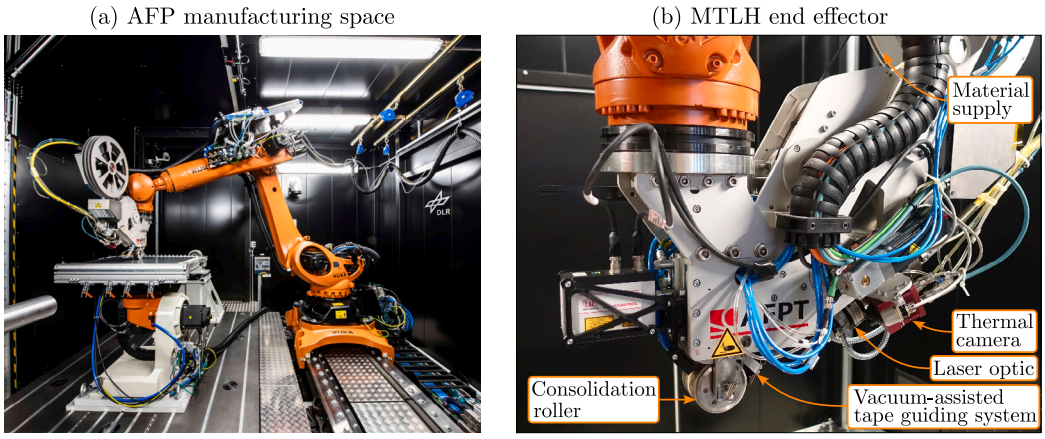

Fig. 1. Thermoplastic tape placement facility.

Table 3
AFP manufacturing parameters [35].

Layup speed [mm/s]	125
Consolidation force [N]	500
Tool set temperature [°C]	20
Nip point set temperature [°C]	470
Tape tension [N]	15

of simultaneously processing up to three 12.7 mm (0.5 inch) wide thermoplastic tapes. Consolidation was achieved using a water-cooled steel roller (60 mm width, 80 mm diameter) with a 5 mm thick outer layer of 60 Shore A silicone, applying a consistent compaction force of 500 N resulting in a peak pressure of 10 bar. A vacuum-assisted tape guiding system, developed in-house at DLR, was implemented to enhance layup accuracy through extended tape guidance post-cut and delayed fold-down. Single tow layup of 12.7 mm tape was performed using a 6 kW near-infrared diode laser heat source (Laserline GmbH, Muelheim-Kaerlich, Germany) coupled with an OTS-1 optic, generating a 40 mm × 20 mm focal spot at a 242 mm working distance. Substrate and tape surface temperatures were continuously monitored via an infrared sensor array, forming a closed-loop control system to regulate laser power and incidence angle, maintaining process parameters within an optimized range. While absolute temperature values were not determined (assuming a thermal emissivity of $\varepsilon_e = 1$), temperature deviations from the optimized process window were reliably identified. The AFP process parameter set used in this work was established through prior research [35] and is detailed in Table 3. While a heated tooling yields better consolidation results and mechanical properties, the unheated tooling configuration was chosen as steered samples were compared with straight layup within a closed dataset. AFP process parameters likely affect the steering results but were kept constant at the optimized values for straight layup. As the introduction of further variables would have exceeded the scope of the available experimental resources, the focus was placed on the geometric influencing factors. AFP-grade 12.7 mm wide CF/LM-PAEK prepreg tape (Suprem SA, Yverdon-les-Bains, Switzerland) with 0.19 mm unprocessed tape thickness and 55 % fiber volume fraction was used for the experiments.

2.2. Laminate design

Two-ply substrates were fabricated for the first set of steering experiments. The initial ply consisted of mechanically fastened wide prepreg tape oriented at 90°, joined on the tool-facing side with polyimide adhesive tape to create a full layer. This was followed by a 0° ply of half-inch tape. Steering experiments then utilized individual tow tracks of the same half-inch material, placed on the substrate beginning with a 150 mm straight lead-in path at 0° . A series of steering radii were investigated, ranging from 2000 mm to 200 mm in 200 mm decrements, and from 800 mm to 200 mm in 50 mm decrements. One track was produced for each radius. To assess process variability, 22 samples were manufactured at a steering radius of 1200 mm in a second experiment.

To investigate the relationship between in-plane path curvature and consolidation quality of in-situ AFP laminates, laminates with steered plies were manufactured and tested. Steering radius and arc length were systematically varied to assess the influence of curvature at different stages. The same mechanically fastened first ply system was employed for the steering laminates. The laminates were fabricated with two steering radii — 1250 mm and 2500 mm — to investigate the effect of in-plane curvature on laminate consolidation and mechanical performance. For each radius, two arc lengths were selected, resulting in four distinct steering parameter sets. The longer arc length for each radius was chosen to be just below the critical arc length, as determined in the first set of experiments, thereby maximizing curvature while maintaining consolidation quality. Ten plies of alternating curvature, with 50 % staggering between successive plies of the same curvature direction, were laid up on an initial 0° ply prepreg layer using half-inch wide prepreg tape and the optimized AFP parameters detailed in Table 3. Layup paths were designed to be tangential to the 0° direction at the specimen center (Fig. 2).

Lateral track spacing was adjusted to eliminate gaps or overlaps at the specimen center. While this resulted in minor gaps and overlaps outside the central region, it maximized the number of identical specimens with consistent local path curvatures. A final 0 ° ply was added for symmetry, resulting in a ply stacking sequence of $[0/(-\theta/+\theta)_5/0]$. The local fiber angle (θ_f) is a function of the distance from the symmetry plane (y_0) and the steering radius (R), as defined by:

$$\theta_f(R, y_0) = \sin^{-1}\left(\frac{y_0}{R}\right) \tag{5}$$

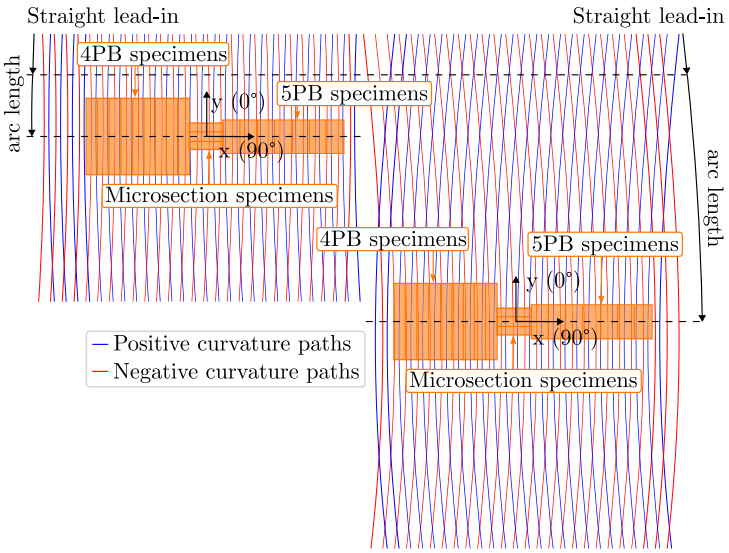

Fig. 2. Steering laminate design with example layup paths and specimen positions.

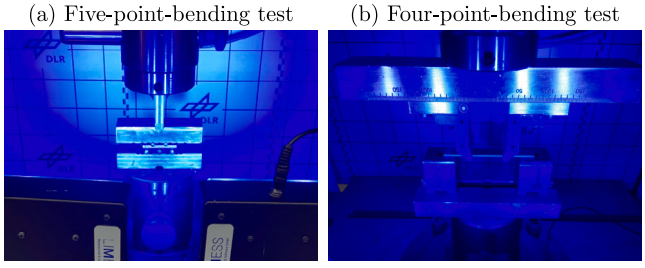

Fig. 3. Mechanical test setups with DIC.

Table 4
Experimental design of steering laminates.

Specimen label	Steering radius	Arc length
R2500-A300	2500 mm	300 mm
R2500-A75	2500 mm	75 mm
R1250-A150	1250 mm	150 mm
R1250-A75	1250 mm	75 mm
UD Ref	–	–

For the five- and four-point bending specimens, maximum distances from the symmetry plane were 20 mm and 46 mm, respectively, resulting in maximum local fiber angles of ±0.9° and ±2.1° . This stacking sequence thus approximated an almost unidirectional laminate while capturing the effects of steering on consolidation. A unidirectional laminate with stacking sequence $[0]_{12}$ served as a reference. The experimental design for the steering laminates is summarized in Table 4.

2.3. Analysis methods

Process data was recorded throughout all manufacturing experiments. The steering tracks were characterized via visual inspection, profilometry, and caliper measurements to determine consolidated tape width and flexible ruler measurement to analyze the respective arc lengths. Out-of-plane defects were defined as over-folding of the tape, resulting in a local thickness increase, the position of which could be determined by visual analysis.

An initial assessment of steering laminate consolidation quality was performed using ultrasonic inspection with an Evident (formerly Olympus, Tokyo, Japan) OmniScan MX2 phased array system equipped

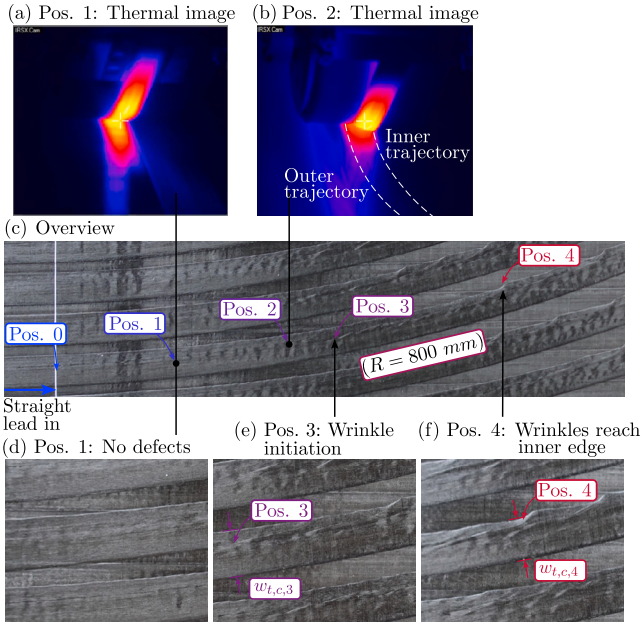

Fig. 4. Steering experiment example image with steering radius 800 mm.

with a 5L64-NW1 probe. A 5 MHz frequency was selected for its prevalence in composite material characterization. System parameters, including voltage (40–115 V) and gain (0–3 dB), were adjusted to achieve an 80–90% full-screen height back wall echo on the A-scan display, ensuring sufficient signal penetration without excessive front-wall amplification, as per ASTM E1001 standard [36].

Following non-destructive evaluation, microsection and mechanical test specimens were extracted from the laminates at the locations indicated in Fig. 2 using water jet cutting. The long side of all rectangular mechanical test samples was orientated in the y-direction (0°), whereas the section plane of the microanalysis specimens was oriented in the x-direction (90°). For microstructural analysis, specimens were embedded in epoxy resin and prepared using a Struers ApS (Ballerup, Denmark) grinding and polishing system. A two-stage grinding process was followed by a three-stage polishing process employing 9, 3, and 0.25 µm diamond suspensions. Micrograph images were acquired using

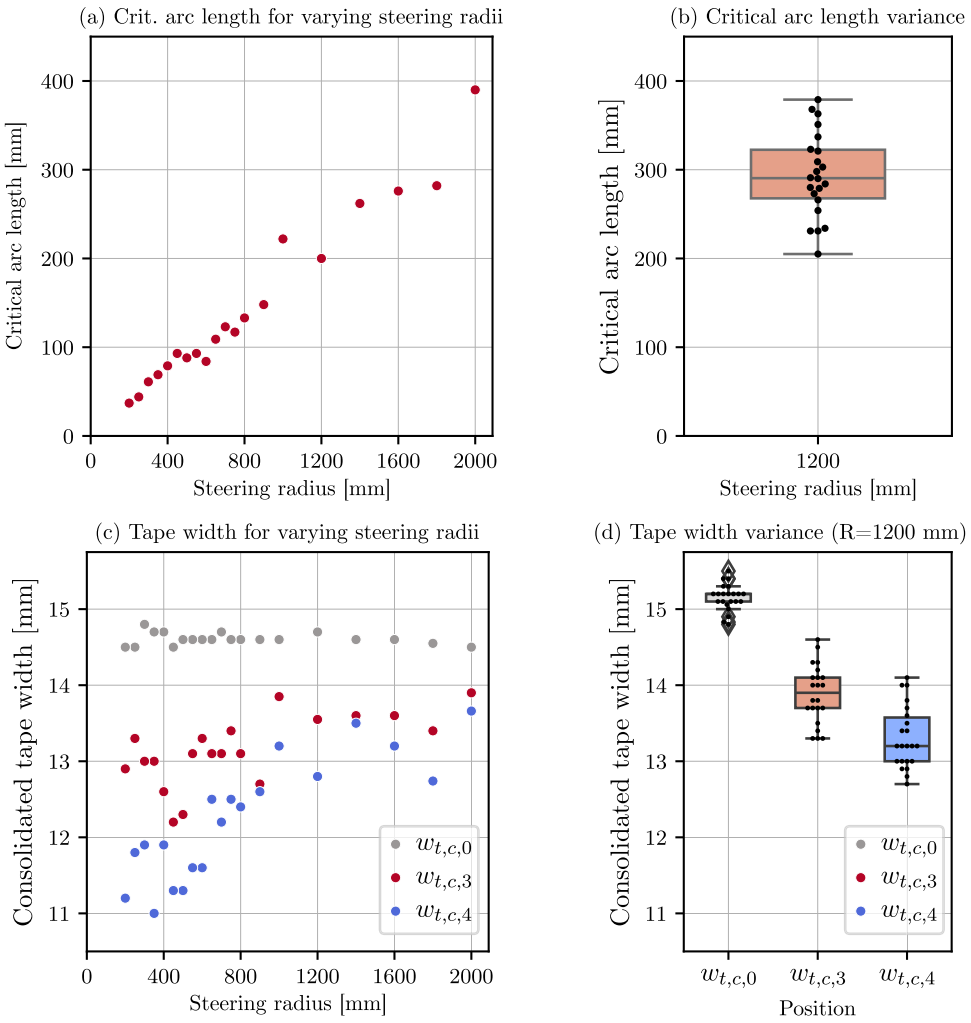

Fig. 5. Critical arc length and tape width measurement results.

a Keyence Corporation (Osaka, Japan) VHX-5000 digital microscope at 500× magnification.

Mechanical properties were determined using four-point and five-point bending tests. While three-point bending tests are commonly used to assess interlaminar shear strength (ILSS), their applicability to thermoplastic materials is limited due to the non-standard ductile failure mode and superposition of flexural strength and ILSS. Therefore, four- and five-point bending tests were employed in this work to independently quantify these properties, providing a more nuanced understanding of the impact of in-plane path curvature on the mechanical performance of the AFP laminates. Digital Image Correlation (DIC) was employed for full-field strain measurement and to facilitate the identification of damage initiation and failure modes. ILSS was determined using five-point-bending testing, following the procedure outlined in ISO 19927 [37]. This configuration, also known as a double-beam shear test, promotes relevant in-plane shear failure in ductile thermoplastic materials. Rectangular specimens (40 mm × 20 mm) were tested with a span-to-thickness ratio of 5, using 6 mm diameter cylindrical supports. Testing was conducted on a ZwickRoell 100 kN universal testing machine with a 100 kN load cell at a crosshead speed of 0.5 mm/min until significant delamination was observed. The interlaminar shear stress (τ) was calculated using the following equation:

$$\tau = \frac{33 \cdot P}{64 \cdot w \cdot t_n} \tag{6}$$

where P is the applied force, w is the specimen width, and t_n is the specimen thickness. Crack initiation was defined as the point of maximum acceleration of the shear strain rate, determined from DIC analysis of the principal shear regions.

Flexural properties, including strength, stiffness, and modulus, were assessed using four-point-bending, following ASTM D7264 [38]. Specimens (92 mm × 13 mm) were tested with a span-to-thickness ratio of 32 (70 mm span), employing 6 mm diameter supports and loading noses. Tests were conducted on the ZwickRoell 100 kN machine with a 100 kN load cell at a crosshead speed of 1 mm/min until failure. Mid-span deflection (δ) was measured using DIC.

Maximum strain at the outer surface (ε_b) and stress (σ_b) were calculated as follows:

$$\varepsilon_b = \frac{4.36 \cdot \delta \cdot t_n}{L^2} \tag{7}$$

$$\sigma_b = \frac{3 \cdot P \cdot L}{4 \cdot w \cdot t_n^2} \tag{8}$$

where P is the applied force, L is the support span (70 mm), t_n is the specimen thickness and w is the specimen width.

The flexural modulus of elasticity (E_b) was calculated from the slope of the stress–strain curve in the linear elastic region (between 0.001 and 0.003 strain), determined from DIC measurements:

$$E_b = \frac{\Delta\sigma}{\Delta\varepsilon} \tag{9}$$

Specimen surfaces were prepared for Digital Image DIC analysis by applying a random speckle pattern using white and black spray paint. The resulting mean speckle diameter of 50 μm was less than half the

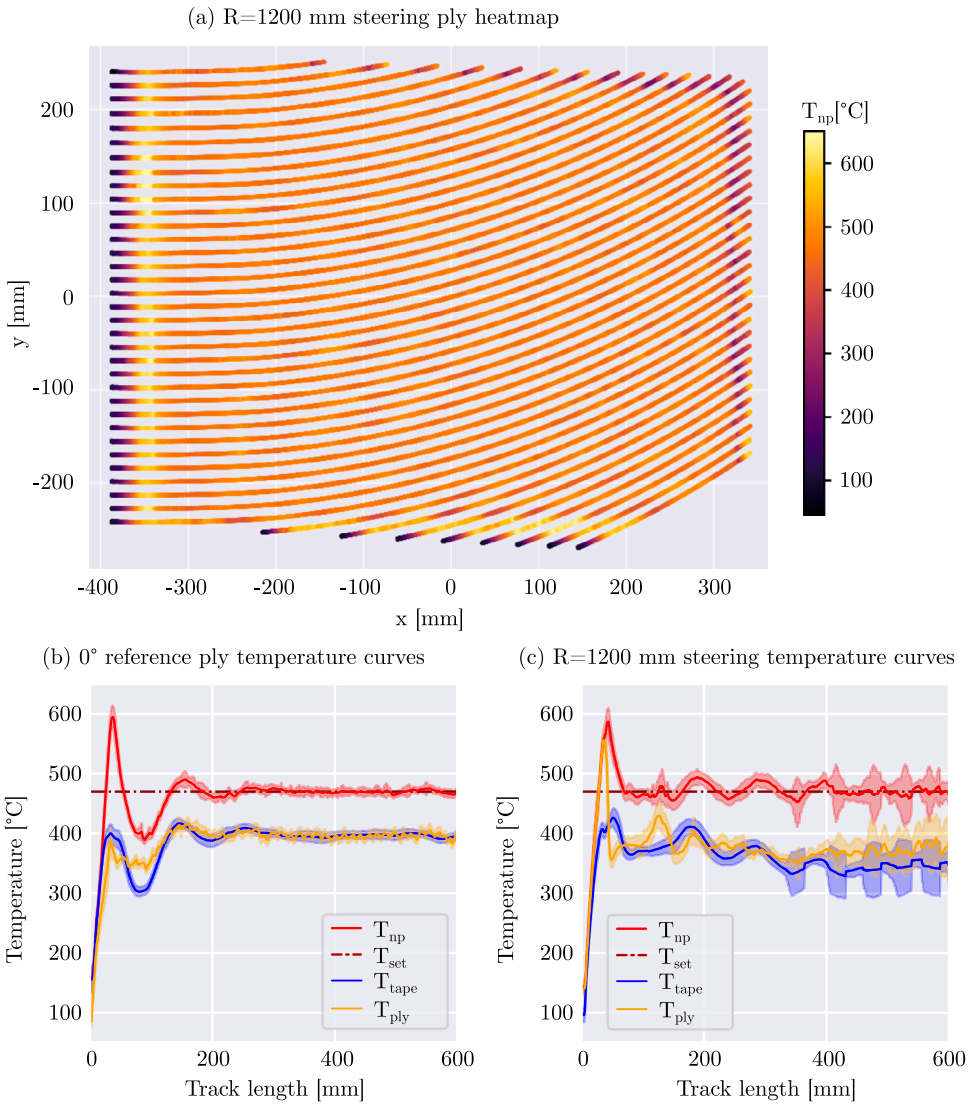

Fig. 6. Heatmap and average track temperature curves of steering and straight reference experiments as measured by thermal camera at thermal emissivity $\varepsilon_e = 1$.

layer thickness (125 μm) and allowed for accurate detection of cracks and delaminations. A LIMESS Messtechnik & Software GmbH (Krefeld, Germany) Q400 DIC system was employed, operating at a frame rate of 5 fps. Virtual measurement surfaces were defined within the free lengths of the specimens to facilitate strain evaluation. A schematic of the mechanical test setups is presented in Fig. 3.

2.4. Statistical analysis

All statistical analyses were conducted with a significance level of $\alpha = 0.05$. Prior to analysis, the normality of mechanical test data was verified using the Shapiro–Wilk test, and the equality of variances was assessed using Levene's test. Statistical significance between parameter sets was determined using a t-test for two-group comparisons or one-way ANOVA for three or more groups, followed by Tukey's post-hoc test for pairwise comparisons. Tukey's test was employed to control for Type I error due to multiple comparisons. The limiting factor of the statistical model is the relatively small number of samples (n = 8), which is typical for mechanical tests. Small and medium effects can therefore remain undetected (type II error). Data visualization and statistical analysis were performed using Python with the NumPy, pandas, statsmodels, SciPy, Matplotlib, and seaborn packages.

3. Results and discussion

3.1. Individual steered tracks

Fig. 4 illustrates the progression of steered tape layup for an example track with a straight lead-in and 800 mm steering radius. Initial sections of the steered path (Position 0–1) exhibited no visible defects, corroborated by thermal camera imaging (Fig. 4(a)). Beginning at Position 1, minor in-plane and out-of-plane undulations were observed. At Position 2, the tape began to detach from the consolidation roller along the inner edge (Fig. 4(b)), followed by the formation of the first out-of-plane wrinkle at Position 3 (Fig. 4(e)). This wrinkle morphology, resembling a "sheared fiber" defect, as documented in thermoset AFP literature [17], propagated in the layup direction towards the inner radius at Position 4 (Fig. 4(f)). The onset of the out-of-plane wrinkle defects was identified via visual inspection as over-folding of the tape and the arc length position was measured using the flexible ruler. This over-folding criterion was selected over an out-of-plane wrinkle amplitude threshold as it characterizes a clear and unambiguous definition of the defect, whereas out-of-plane waviness could also be caused by steering-independent effects such as gaps or overlaps in the previous layer. Up to Position 4, a steady decrease in consolidated tape width was observed, which sharply increased as the wrinkle reached the inner

edge. Subsequently, periodic out-of-plane wrinkle defects formed and propagated towards the inner edge.

The arc length from Position 0 to Position 3 was defined as the critical arc length, l_{crit}, marking the initiation of out-of-plane defect formation. While in-plane and out-of-plane undulations occur before this critical arc length, these defects did not disrupt the ply composition and the layup of the following plies to the same degree as the wrinkle defects. The wrinkle defects also marked the onset of more severe shear deformation of the tape resulting in deviations of the inner tape edge from a predictable trajectory. Consolidated tape widths at Positions 0, 3, and 4 were designated as $w_{t,c,0}$, $w_{t,c,3}$ and $w_{t,c,4}$, respectively. A similar progression of steering and defect formation was consistently observed across all steering radii, although the magnitude of the critical arc length l_{crit} varied.

The qualitative observation as described above thus agrees with the hypothesis of the transient build-up of stresses in the tape in front of the consolidation roller until a critical value is reached at which the out-of-plane defects occur. The initiation of the out-of-plane defects as "sheared fiber" defect indicates induced shear stress in the tape in front of the consolidation roller following tensile stress at the outer edge and compressive stress at the inner edge of the tape. A more detailed analysis of the deformation and stresses will be presented in Part 2 of this work.

Fig. 5(a) and (c) present critical arc length results and consolidated tape width measurements at varying steering radii, respectively. Fig. 5(b) and (d) present variance analysis of the second experiment at constant steering radius of 1200 mm. The critical arc length measurements in Fig. 5(a) shows a proportional correlation between steering radius and critical arc length. Larger steering radii allowed for longer defect-free arc lengths during layup. Fig. 5(b) illustrates the variance in critical arc length obtained from multiple iterations of the 1200 mm steering radius. The substantial variance, two orders of magnitude larger than the assumed measurement accuracy of 1 mm, is likely exacerbated by the subjective nature of classifying out-of-plane wrinkle defects used to define the critical arc length, introducing further inaccuracy. The discrepancy in the data sets between the determined critical arc lengths for 1200 mm in Fig. 5(a), 200 mm, and the distribution values in Fig. 5(b) with a median value of 290 mm is probably also due to the subjective classification of the out-of-plane wrinkles, which either consider a smaller wave to be critical, or only a larger wrinkle, resulting in either a smaller or larger value for the critical arc length, respectively. This is a disadvantage of the critical arc length criterion, which, however, similarly pertains to the critical radius as defined in the literature, which also depends on visual inspection and subjective classification of out-of-plane defects.

Fig. 5(c) presents consolidated tape width caliper measurements ($w_{t,c,0}$, $w_{t,c,3}$, and $w_{t,c,4}$) for varying steering radii. The initial tape width at the end of the straight lead-in section ($w_{t,c,0}$) remained consistent across all radii, exhibiting minimal variation with a standard deviation of 0.17 mm (Fig. 5(d)). In contrast, both $w_{t,c,3}$ and $w_{t,c,4}$ exhibited greater deviation. A clear correlation between steering radius and consolidated tape width was observed; smaller steering radii consistently resulted in narrower tape widths. This narrowing effect was approximately three times more pronounced at Position 4 $w_{t,c,4}$ compared to Position 3 ($w_{t,c,3}$), suggesting increased geometrical deformation as the wrinkles propagated towards the inner edge. A discrepancy between the two data sets between the radius-dependent measurements (Fig. 5(c)) and the variance analysis at constant radius (Fig. 5(d)) can also be seen in the tape width analyses. In this case, the caliper measurement is not expected to have a large influence on the error. The difference in tape widths before steering ($w_{t,c,0}$) therefore indicates a deviating process window. As the process parameters (Table 3) were kept constant, it is not possible to conclusively clarify the cause of the deviation. One possible explanation would be a slight degradation of the consolidation roller at the time of the second experiment, which made the silicone harder and resulted in a higher effective maximum consolidation pressure and thus larger consolidated tape width. These first two experiments, however, show the coherence between steering radius, critical arc length and tape width progression.

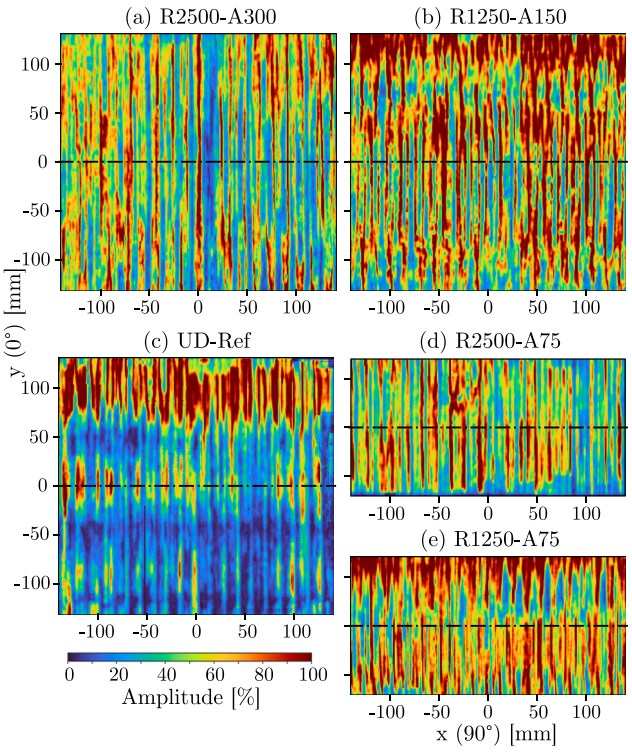

Fig. 7. Ultrasonic C-scan results of steered and unidirectional laminates.

Process temperatures during the layup of the steered tracks were monitored using the system's integrated thermal camera (assuming emission coefficient $\varepsilon_e = 1$). While the camera does not directly measure nip point temperature (T_{np}), deviations from the set point (T_{set}) of 470 °C were analyzed. The thermal heatmap for a 1200 mm radius steering ply (Fig. 6(a)) demonstrates an initially stable temperature distribution after the transient start of the track. The current temperature control strategy relies on brief temperature overshoots to reach the target temperature, with these sections deliberately positioned outside the final laminate trim line. A comparative analysis of average temperature profiles for straight (Fig. 6(b)) and curved tracks (Fig. 6(c)) reveals the influence of curvature on process temperatures. While the system effectively matched the temperature of the incoming tape (T_{tape}) and the substrate temperature (T_{ply}) and maintained close adherence to the target temperature for 0° reference tracks, greater temperature deviations were observed in the curved tracks. The representative 1200 mm radius steering ply exhibited increased temperature variance after approximately 300 mm (the critical arc length). This increased variance coincided with the onset of severe out-of-plane wrinkling, which further destabilized temperature control due to recurring fluctuations in tape temperature. Consequently, sections exceeding the steering-radius-dependent critical arc length, characterized by out-of-plane wrinkles, fluctuating tape widths, and unstable process temperatures (T_{tape} and T_{ply}), are deemed unsuitable for inclusion in the final laminate.

3.2. Steering laminates

Nip point temperature analysis demonstrated consistent and uniform temperatures throughout the steered plies. Table 5 summarizes the median nip point temperatures calculated for areas corresponding to the mechanical test specimen locations. Specimens with a 75 mm arc length exhibited greater temperature variance, likely due to the

Fig. 8. Microsections of steered and unidirectional laminates.

Table 5
Median and standard deviation of nip point temperatures in areas corresponding to mechanical test specimen locations.

Specimen label	Steering radius	Arc length	4PB T_{np} [°C]	5PB T_{np} [°C]
R2500-A300	2500 mm	300 mm	470.9 ± 6.6	470.8 ± 6.3
R2500-A75	2500 mm	75 mm	468.0 ± 33.6	466.4 ± 10.4
R1250-A150	1250 mm	150 mm	475.9 ± 7.3	477.8 ± 7.2
R1250-A75	1250 mm	75 mm	470.5 ± 10.2	468.3 ± 5.7
UD Ref	–	–	469.5 ± 15.9	466.2 ± 10.8

proximity of these areas to the transient sections at the beginning of each track. A slightly elevated median temperature was observed in the R1250-A150 specimen area, corresponding to the most demanding steering configuration with the smallest radius and longest arc length. However, statistical analysis revealed no significant differences in nip point temperatures between the specimen groups, indicating a robust and consistent consolidation process.

Fig. 7 presents ultrasonic C-scan results obtained from the backwall of the steered and unidirectional laminates. Longitudinal patterns in vertical orientation corresponding to the layup direction were observed across all laminates. The orientation of the patterns suggests that they occur at the respective tape edges between the individual tracks due to the porosity present there, which in turn is caused by slight gaps or overlaps between the tracks due to the consolidated tape width not being set optimally. Notably, the R1250 laminates (Fig. 7(b) and (e)) exhibited the largest areas of high-amplitude backwall echo, suggesting a more complete consolidation and closer alignment between the layup path and consolidated tape width in these sections. Unexpectedly, the unidirectional reference laminate displayed substantial regions of low-amplitude backwall echo, potentially indicating a slight mismatch of layup paths and consolidated tape width.

Fig. 8 presents representative microsections of the steered and unidirectional laminates. The unidirectional laminate exhibited generally good consolidation, with only minor, scattered intralaminar pores (Fig. 8(a)). Tow-to-tow boundaries were clearly defined by matrix-rich regions, but exhibited no apparent porosity. Similar well-defined boundaries were observed in the steered laminates (Fig. 8(b)–(e)), with the exception of the R2500-A300 sample, which displayed gaps in several plies, potentially indicating an overestimation of consolidated tape

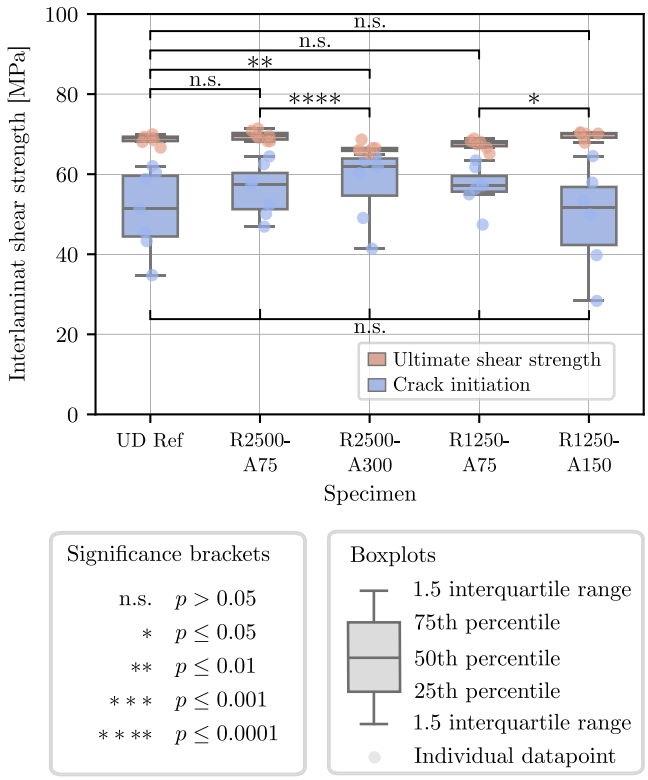

Fig. 9. Five-point bending test results.

width. An example gap defect can be seen in the center of the fourth ply from the top of Fig. 8(b). As expected, greater variation in consolidated tape width was observed in the advanced arc length sample (R2500-A300). Notably, despite this variation, porosity at the tow boundaries was minimal due to the near-0° ply orientation, facilitating smooth merging of adjacent plies. However, the R1250 specimens revealed pronounced intralaminar porosity, particularly within ply 4.

Fig. 9 presents the results of the five-point bending tests, quantifying the interlaminar shear strength (ILSS) of the steered and unidirectional laminates. Statistical analysis, including Shapiro–Wilk and Levene's tests, confirmed the normality and comparability of variances, enabling the use of independent t-tests and one-way ANOVA with Tukey's post-hoc test for pairwise comparisons. Significance brackets in the figure indicate statistical significance.

While crack initiation results exhibited high variance and no significant differences, ultimate strength measurements demonstrated good reproducibility, with a consistent standard deviation of approximately 1 MPa across all specimen groups. No statistically significant difference was observed between the unidirectional reference and any steered specimen group, with the exception of the R2500-A300 specimens, which exhibited a 4.3% reduction in strength compared to the reference. This decrease correlates with the slightly suboptimal consolidated tape width observed in the R2500-A300 specimens, as confirmed by microsection analysis. Similarly, comparing specimens within the R2500 radius group revealed a 5% strength decrease between the A75 and A300 specimens, potentially attributable to the observed gap defects in the longer arc length samples. In contrast, the R1250 specimens showed a slight 3.1% increase in strength between the A75 and A150 samples, although this difference exhibited a relatively high p-value of 0.02, suggesting lower statistical significance. Larger porosity as observed in the R1250-A75 specimens (Fig. 8(e)) did not have an effect on the shear strength results which could be attributed to the large ductility of the LM-PAEK matrix.

Fig. 10 presents the results of the four-point bending tests, illustrating the ultimate strength and modulus of the steered and unidirectional laminates. Prior to statistical analysis, the normality and comparability of variances were confirmed using the Shapiro–Wilk and Levene's tests, respectively. Statistical comparisons revealed a significant increase in ultimate strength for the R2500-A75 specimen group, exhibiting an 18.4% improvement compared to the unidirectional reference. A reduction in bending modulus was observed for the longer arc length specimen groups, with decreases of 3.5% for the R2500 samples and 10.0% for the R1250 samples. This decrease is in bending modulus likely attributable to fiber undulations induced by the progressed arc length. As observed in the visual inspection of individual steered tracks (Fig. 4), in- and out-of-plane waviness gradually increase with increasing arc length until a critical out-of-plane wrinkle occurs at the critical arc length. The longer arc length samples therefore have a higher proportion of in- and out-of-plane undulations in the fibers of all curved layers. Due to the undulations, the lower layers of the laminate subjected to tensile stress and the upper layers subjected to compressive stress have less tensile and compressive stiffness, respectively, which leads to a reduced overall bending stiffness of the samples. Future work will elaborate on these mechanical test results and aim to quantify the in- and out-of-plane fiber waviness as a function of radius of curvature and arc length to analyze the correlation with mechanical stiffness properties.

Overall, these results demonstrate that adequate consolidation quality can be maintained with steering radii up to the critical arc length. This work was specifically aimed at demonstrating that steering radii smaller than the traditionally defined critical steering radius can be employed for the in-situ AFP process. In all experiments reported here, the arc length was deliberately chosen to remain below the critical arc length—defined herein as the point at which the first out of plane wrinkle appears. The absence of any out of plane defects and the retention of controllable tape boundaries allows for the laminate to remain without severe defects, such as gaps and overlaps between adjacent steered tapes with uncontrolled tape boundaries or significant out-of-plane wrinkles. Accurate prediction of steering-induced geometric changes is crucial to optimize tow-to-tow spacing and consolidated tape width, thereby minimizing the potential for defects. In contrast, when the arc length exceeds the critical value, the tape width shows a pronounced variance (Fig. 5(d)), the in- and out-of-plane undulations become severe (Fig. 4(f)) and the temperature control system can no longer keep the process temperature within the optimal range (Fig. 6(c)). These distortions translate directly into gap or overlap defects in the laminate and since in-situ AFP does not employ a post consolidation process step the defects cannot be mitigated and remain embedded in the final part.

Thus, the critical arc length serves as a practical guideline for selecting steering parameters that guarantee defect free, controllable tape placement for in-situ AFP. While a dedicated set of laminates fabricated with arc lengths longer than the critical arc length was not included, the observed trend in geometric data supports the notion that the critical arc length is a meaningful threshold for preventing detrimental defects in in-situ AFP. Future work will address this directly by fabricating and testing laminates with arc lengths beyond the critical value to quantify the precise impact on mechanical performance and to refine the critical arc length definition.

The critical arc length principle has practical relevance to AFP part manufacturing and can help to guide the design of the manufacturing process. It allows for short sections with large local in-plane curvature, as long as the arc length remains below the critical arc length for the respective curvature. This significantly increases the design space for real complex geometry applications. Small areas with strong curvature can be specifically evaluated and a defect-free layup strategy that utilizes the full potential of the in-situ AFP process can be created. The critical arc length criterion thus presents a usable design principle for layup strategies for complex geometries.

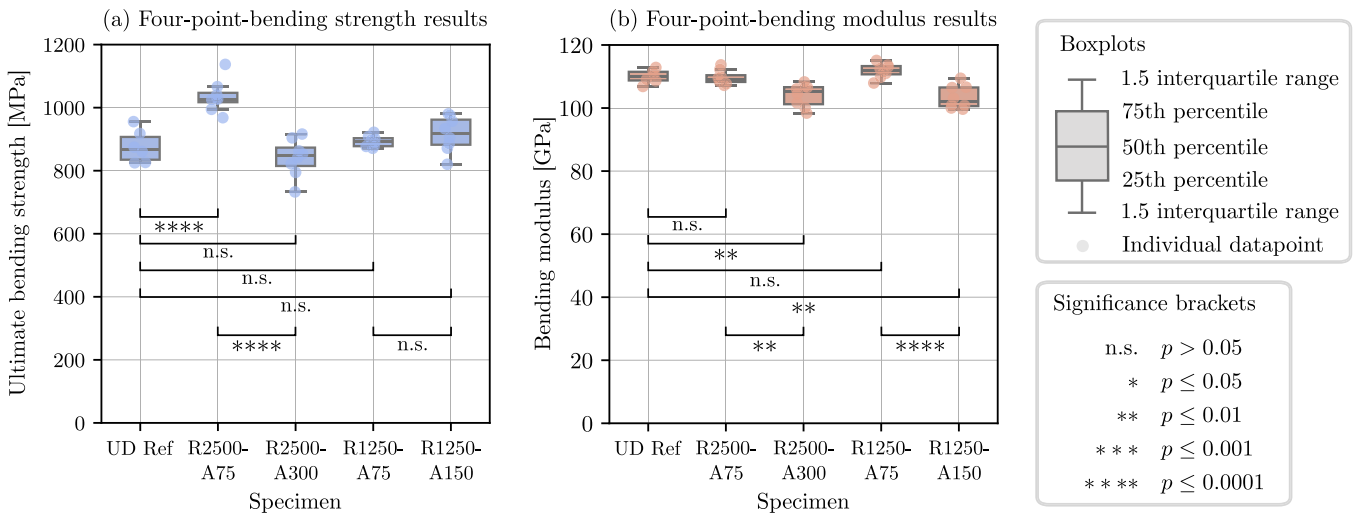

Fig. 10. Four-point bending test results showing ultimate strength and modulus.

4. Conclusion

This research presents a comprehensive investigation into the influence of constant geodesic curvature (steering) on the mechanical performance of laminates manufactured via in-situ Automated Fiber Placement. The progression of steered layup paths was characterized, alongside the identification and analysis of steering-induced defects and their impact on process temperature and microstructure. A novel concept of critical arc length was developed to define the limits of successful steering in in-situ AFP. The results demonstrate that steering radii previously considered too small can be effectively utilized up to a radius-dependent critical arc length. Coupon-level mechanical testing of interlaminar properties, considered critical for the in-situ AFP process, revealed minimal effects of steering on interlaminar shear and bending strength. However, a reduction in bending modulus of up to 10% was observed in steered specimens approaching the critical arc length, attributed to steering-induced fiber undulations and increased flexural compliance. These findings contribute to a better understanding of steering in in-situ AFP and provide guidance for optimizing process parameters and laminate design.

Part 2 of this work investigates the dimensional changes of steered tape, accounting for narrowing of the consolidated tape width along the steered path and derives optimized layup strategies to avoid coverage defects between narrowing steered tapes. Future work will investigate the impact of AFP process parameters such as layup speed and nip point temperature on the critical arc length. Based on the results of this work and Part 2, optimized laminates with curved paths will be produced and tested at subcomponent level.

CRediT authorship contribution statement

Lukas Raps: Writing – original draft, Visualization, Methodology, Investigation, Formal analysis, Data curation, Conceptualization. **Ashley R. Chadwick:** Writing – review & editing, Validation, Supervision. **Heinz F. Voggenreiter:** Writing – review & editing, Supervision, Resources.

Declaration of competing interest

The authors declare that they have no known competing financial interests or personal relationships that could have appeared to influence the work reported in this paper.

Acknowledgments

This research work is part of the project FFS (Fortschrittliche Flugzeugstrukturen) which is financially supported by the German Federal Ministry of Defence.

Data availability

Data will be made available on request.

References

[1] Chadwick AR, Doll G, Christ U, Maier S, Lansky S. Performance of in-situ automated fibre placement parts. Composites A 2025;192:108725.
[2] Tam AS, Gutowski TG. The kinematics for forming ideal aligned fibre composites into complex shapes. Compos Manuf 1990;1(4):219–28.
[3] Land IB. Design and manufacture of advanced composite aircraft structures using automated tow placement (Ph.D. thesis).
[4] Wang H, Chen J, Fan Z, Xiao J, Wang X. Experimental investigation on the influence of fiber path curvature on the mechanical properties of composites. Comput Struct 2021;14(10):2602.
[5] Oya N, Johnson DJ. Longitudinal compressive behaviour and microstructure of PAN-based carbon fibres. Carbon 2001;39(5):635–45.
[6] Zenker T. Einfluss prozessspezifischer designparameter des thermoplastischen automated fiber placements auf die bauteilqualität in abhängigkeit der prozesskette (Ph.D. thesis).
[7] Belhaj M, Hojjati M. Wrinkle formation during steering in automated fiber placement: Modeling and experimental verification. J Reinf Plast Compos 2018;37(6):396–409.
[8] Zenker Thomas, Schwab M. Analysis of fiber steering effects in thermoplastic automated fiber placement. In: ECCM18 - 18th European conference on composite materials. 2018.
[9] Pan H, Yang D, Qu W, Li J, Ke Y. Process-dependent wrinkle formation for steered tow during automated fiber placement: Modeling and experimental verification. Thin-Walled Struct 2022;180:109928.
[10] Peeters DM J, Lozano GG, Abdalla MM. Effect of steering limit constraints on the performance of variable stiffness laminates. Comput Struct 2017;196(2):94–111.
[11] Smith RP, Qureshi Z, Scaife RJ, El-Dessouky HM. Limitations of processing carbon fibre reinforced plastic/polymer material using automated fibre placement technology. J Reinf Plast Compos 2016;35(21):1527–42.
[12] Blom A, Stickler P, Gurdal Z. Design and manufacture of a variable-stiffness cylindrical shell. In: Proceedings of the SAMPE europe 30th international conference. 2009.
[13] Blom AW, Tatting BF, Hol JMAM, Gürdal Z. Fiber path definitions for elastically tailored conical shells. Composites B 2009;40(1):1.
[14] Akbarzadeh AH, Nik MA, Pasini D. The role of shear deformation in laminated plates with curvilinear fiber paths and embedded defects. Compos Struct 2014;118(12):217–27.
[15] Blom AW. Structural performance of fiber-placed, variable-stiffness composite conical and cylindrical shells (Ph.D. thesis).

[16] Nik MA, Fayazbakhsh K, Pasini D, Lessard L. Optimization of variable stiffness composites with embedded defects induced by automated fiber placement. Compos Struct 2014;107(1):160–6.
[17] Bakhshi N, Hojjati M. An experimental and simulative study on the defects appeared during tow steering in automated fiber placement. Composites A 2018;113:122–31.
[18] Hörmann PM. Thermoset automated fibre placement – on steering effects and their prediction (Ph.D. thesis), Technische Universität München.
[19] Matveev MY, Schubel PJ, Long AC, Jones IA. Understanding the buckling behaviour of steered tows in automated dry fibre placement (ADFP). Composites A 2016;90:451–6.
[20] Rajan S, Sutton MA, Wehbe R, Tatting B, Gürdal Z, Kidane A, Harik R. Experimental investigation of prepreg slit tape wrinkling during automated fiber placement process using StereoDIC. Composites B 2019;160:546–57.
[21] Zhao C, Xiao J, Huang W, Huang X, Gu S. Layup quality evaluation of fiber trajectory based on prepreg tow deformability for automated fiber placement. J Reinf Plast Compos 2016;35(21):1576–85.
[22] Wei T, Qu W, Yang D, Ke Y. Understanding and controlling wrinkle formation under time–process interactions during automated fiber placement (AFP) steering. Composites A 2025;199:109214.
[23] Wehbe R, Sacco C, Baz Radwan A, Albazzan M, Harik R. Influence of process parameters in AFP fiber steering on cylinders: Constant curvature paths. Composites C 2020;2:100036.
[24] Beakou A, Cano M, Le Cam J-B, Verney V. Modelling slit tape buckling during automated prepreg manufacturing: A local approach. Compos Struct 2011;93(10):2628–35.
[25] Kheradpisheh M, Hojjati M. In-plane and out-of-plane deformations in automated fiber placement employing micromechanics method. Composites A 2023;170:107543.
[26] Wehbe R, Tatting B, Rajan S, Harik R, Sutton M, Gurdal Z. Geometrical modeling of tow wrinkles in automated fiber placement. Compos Struct 2020;246.
[27] Wang Y, Mahapatra S, Belnoue JP-H, Ivanov DS, Hallett SR. Modelling the effect of process conditions on steering-induced defects in automated fibre placement (AFP). Composites A 2023;173:107702.
[28] Wu K, Tatting B, Smith B, Stevens R, Occhipinti G, Swift J, Achary D, Thornburgh R. Design and manufacturing of tow-steered composite shells using fiber placement. In: 50th AIAA/aSME/ASCE/AHS/aSC structures, structural dynamics, and materials conference. 2012.
[29] Kim BC, Hazra K, Weaver P, Potter K. Limitations of fibre placement techniques for variable angle tow composites and their process-induced defects. In: Proceedings of the 18th international conference on composite materials (ICMM18), Jeju, Korea. 2010, p. 21–6.
[30] Kim BC, Potter K, Weaver PM. Continuous tow shearing for manufacturing variable angle tow composites. Composites A 2012;43(8):1347–56.
[31] Kim BC, Weaver PM, Potter K. Manufacturing characteristics of the continuous tow shearing method for manufacturing of variable angle tow composites. Compoistes A 2014;61:141–51.
[32] Zenker T, Gnaedinger M. Consolidation behavior of fiber steered thermoplastic automated fiber placement preforms. In: 5th international conference & exhibition onthermoplastic composites. 2020.
[33] Clancy G, Peeters D, Oliveri V, Jones D, O'Higgins RM, Weaver PM. A study of the influence of processing parameters on steering of carbon fibre/PEEK tapes using laser-assisted tape placement. Composites B 2019;163(4):243–51.
[34] Rajasekaran A, Shadmehri F. Steering of carbon fiber/PEEK tapes using hot gas torch-assisted automated fiber placement. J Thermoplast Compos Mater 2022;08927057211067962.
[35] Raps L, Chadwick AR, Schiel I, Schmidt I. CF/LM-PAEK: characterisation and sensitivity to critical process parameters for automated fibre placement. Compos Struct 2022;284:115087.
[36] ASTM International and Subcommittee: E0706. ASTM E1001-21 standard practice for detection and evaluation of discontinuities by the immersed pulse-echo ultrasonic method using longitudinal waves. 2021, https://www.astm.org/e1001-21.html.
[37] International Organization for Standardization and Technical Committee: ISO/TC 61/SC 13. ISO 19927 determination of interlaminar strength and modulus by double beam shear test. 2018, https://www.astm.org/d2344_d2344m-22.html.
[38] ASTM International and Subcommittee: D3004. ASTM D7264 standard test method for flexural properties of polymer matrix composite materials. 2007, https://www.astm.org/d7264_d7264m-21.html.